Multiple-order Imaging for Optical Critical Dimension Metrology using Microscope Characterization

Jing Qin*, Hui Zhou, Bryan M. Barnes, Francois Goasmat, Ronald Dixson, Richard M. Silver
Semiconductor and Dimensional Metrology Division, National Institute of Standards and Technology, 100 Bureau Dr. MS 8212, Gaithersburg, MD USA 20899-8212

ABSTRACT

There has been much recent work in developing advanced optical metrology applications that use imaging optics for optical critical dimension (OCD) measurements, defect detection, and for potential use with in-die metrology applications. We have previously reported quantitative measurements for sub-50 nm CD dense arrays which scatter only the 0th-order specular diffraction component using angle-resolved scatterfield microscopy. Through angle-resolved and focus-resolved imaging, we now measure OCD targets with three-dimensional scattered fields that contain multiple Fourier frequencies. Experimental sensitivity to nanometer scale linewidth changes is presented, supported by simulation studies. A new, more advanced approach to tool normalization is coupled with rigorous electromagnetic simulations and library based regression fitting that potentially enables OCD measurements with sub-nanometer uncertainties for targets that scatter multiple Fourier frequencies.

Keywords: optical metrology, electromagnetic simulation, frequency domain tool normalization, multiple frequency scattering, evaluate sensitivities and uncertainties, phase sensitive measurements

1. INTRODUCTION

Recently, much research has concentrated on advancing optical metrology applications that use imaging optics for critical dimension (CD) measurement, overlay metrology, and defect detection. Reduced target dimensions requiring improved resolution and sensitivity have driven the need to use and analyze the phase and scattered frequency information available when using image-based systems. For some time it has been shown that sensitivity to nanometer scale changes can be observed when measuring critical dimensions of sub-wavelength features or when imaging defects below 20 nm using angle-resolved and focus-resolved optical data [1,2].

To achieve such measurements, a technique was developed at the National Institute of Standard and Technology (NIST), scatterfield microscopy, that combines the best attributes of optical microscopy and scatterometry. The technique provides high magnification imaging, spatial selectivity, and a capability to capture all phase and frequency information within the collection numerical aperture. This platform also enables focus-resolved, angle-resolved and polarization-resolved measurement by engineering illumination and detection.

We have previously used optical imaging methods on a scatterfield platform to perform what are essentially angle-resolved scatterometry measurements that fill the imaging field of view (FOV) for dense linewidth arrays that scatter only the 0th-order specular diffraction component [3,4]. These measurements were focused on acquiring images as a function of angle at certain focus position, using targets similar to those used in scatterometry. These angle scans were parametrically fitted successfully with rigorous regression methods with uncertainties calculated using a simulation library based on physics-based three-dimensional electromagnetic field modeling.

Acceptable quantitative statistical analysis with rigorous agreement between experiment and theory has represented an important advance in image-based optical metrology to realize sub-nanometer scale uncertainty measurements. It could provide a means for CD metrology of very small sub-field targets. The measured field can also be non-repetitive and irregular structures unlike those required for scatterometry. However, the success of optical metrology for patterned targets, not only those limited to a zero-order optical response but also those scattering multiple (or even a continuum of)

* jing.qin@nist.gov; phone 1 301 975-4755; fax 1 301 975-4396; www.nist.gov/pml/div683/grp02/htnsm.cfm

Instrumentation, Metrology, and Standards for Nanomanufacturing, Optics, and Semiconductors VI, edited by Michael T. Postek, Victoria A. Coleman, Ndubuisi G. Orji, Proc. of SPIE Vol. 8466, 84660G
© 2012 SPIE · CCC code: 0277-786/12/$18 · doi: 10.1117/12.946120

Downloaded From: http://proceedings.spiedigitallibrary.org/ on 10/15/2012 Terms of Use: http://spiedl.org/terms

frequency components, is dependent upon the ability to fully characterize the complex imaging optics of the microscope, rigorously model measurements with an acceptable degree of accuracy, and quantitatively address uncertainties in measurements.

Here we present our new approach [5] that enables the rigorous analysis of three-dimensional through-focus and angle-resolved optical images for targets that scatter multiple spatial frequency components and extend the approach to a target with a continuum of scattered frequency content. This imaging method samples the three-dimensional electromagnetic field above and into the sample or target of interest. The technique involves parametric fitting of the three-dimensional scattered field, experimental Fourier domain normalization procedures, and the use of rigorous electromagnetic simulation tools and statistical methods to evaluate sensitivities and uncertainties in the measurement of two- and three-dimensional layouts encountered in critical dimension and contour metrology.

We present a simulation study that develops the basic understanding of measurement sensitivities and uncertainties to give a realistic evaluation of possible experimentally achievable sensitivities using a realistic instrument and sample noise model. A rigorous analysis of optical imaging data is developed using both theoretical and experimental methods, as a comprehensive and quantitative characterization of the optical metrology tool is necessary. Illumination engineering and sophisticated tool normalization are presented for a hardware platform that provides access to a conjugate back focal plane, facilitating experimental rigorous, phase-sensitive measurements of features using the through-focus three-dimensional field data.

2. HARDWARE PLATFORM AND COMPLEX TOOL NORMALIZATION

The scatterfield microscopy technique, which provides full access and control of the angular distribution of the incident light, has been described in detail elsewhere [6,7]. The basic instrument is based on a Köhler illuminated bright field microscope with a large accessible conjugate back focal plane (CBFP). Each point at the conjugate back focal plane maps to a plane wave of illumination at the sample as illustrated in Fig. 1. By scanning an aperture on in the CBFP or using a fixed aperture, we can select the incident angle to realize angle-resolved measurements. Also, polarization states can be defined at the CBFP with respect to the sample and imaging optics. Data are acquired as a function of angle or focus position as illustrated graphically in Fig. 2. A charge coupled device (CCD) image is captured at each angle or focus position. A kernel of each image is averaged into a profile and these are stored as arrays as a function of angle or focus position, then they are concatenated into a single data set for parametric fitting and statistical analysis.

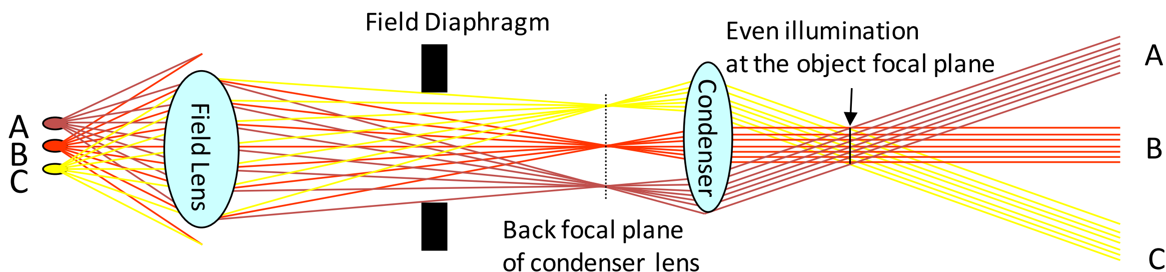

Figure 1. Schematic for a Köhler illuminator. While the general use of Köhler illumination is to illuminate a sample homogeneously even if the source is inhomogeneous, Köhler also permits illumination engineering, such as off-axis illumination, within scatterfield microscopes.

We have previously used scatterfield microscopy to perform essentially angle-resolved scatterometry measurements for dense linewidth arrays which scatter only the specular diffraction component. In such cases, each image is integrated to a single intensity as a function of incident angle. Then the experimental angle-resolved data were normalized by the known reflectance of a reference as a function of angle and polarization, before being parametrically fitted and statistically analyzed. Nanometer scale uncertainties have been obtained [3,8].

Downloaded From: http://proceedings.spiedigitallibrary.org/ on 10/15/2012 Terms of Use: http://spiedl.org/terms

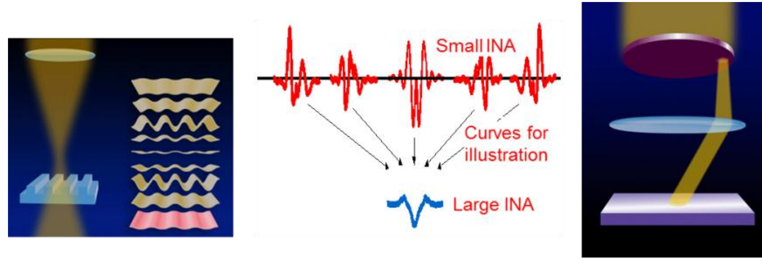

Figure 2. Schematic of the experimental methods for focus-resolved and angle-resolved data acquisition. (left) Information about the target can be collected at various through-focus positions. (center) The use of a low illumination numerical aperture (NA) with incoherent illumination is often preferred to using a large NA which combines the profiles and smears out information content. (right) Specific angles of light can be directed at the surface by engineering the CBFP.

For targets that scatter continuous frequency content or multiple scattering orders, the normalization required to correct the experimental data for instrumentation and hardware errors becomes more complex, since the microscope consists of two groups of optical elements. The illumination path optics determine the light incident on the sample while the collection path optics affect the scattered light transmissivity as a function of angle and polarization. They both introduce instrumentation errors to the image. To implement accurate library-based fitting methods based on electromagnetic scattering simulations, proper experimental normalization procedures combined with rigorous modeling are needed to allow accurate comparison of angle-resolved or focus-resolved measurements with theory.

In practice, this is very complicated when the resulting high order scattered light has scattered spatial frequencies that are continuous, and no simple method exists to isolate and measure the individual orders and normalize them separately. However, since electromagnetic scattering simulations inherently identify the scattering direction of each order, we apply the collection path tool function to the amplitudes of the simulated scattered orders before the image is constructed. Furthermore, the illumination path also needs to be characterized in order to correct the experimental data as the simulations assume unit incident light at each angle and polarization. Thus, both the illumination path tool function and the collection path tool function must be calculated and implemented separately for each individual illumination angle and the resulting vast spectrum of scattered light. Stated differently, the tool must be characterized as a function of polarization and angle over the entire conjugate back plane.

The actual acquisition of the illumination tool function is accomplished by placing a photo diode detector covered by a linearly polarized analyzer at the sample plane and acquiring intensities with the analyzer aligned with the *x* and *y* axes of that plane. Similarly, a polarizer is aligned with the *x* and *y* axes of the CBFP (which corresponds to the sample plane) in the illumination path, yielding four polarizer-analyzer results $I_{PD-xx}(\theta,\varphi)$, $I_{PD-xy}(\theta,\varphi)$, $I_{PD-yx}(\theta,\varphi)$, and $I_{PD-yy}(\theta,\varphi)$, which are determined experimentally using

$$\begin{bmatrix} \sqrt{I_{PD-xx}(\theta,\varphi)} & \sqrt{I_{PD-yx}(\theta,\varphi)} \\ \sqrt{I_{PD-xy}(\theta,\varphi)} & \sqrt{I_{PD-yy}(\theta,\varphi)} \end{bmatrix} = \begin{bmatrix} PD_{SS}(\theta,\varphi) & 0 \\ 0 & PD_{PP}(\theta,\varphi) \end{bmatrix} \cdot \begin{bmatrix} A_{SS}(\theta,\varphi) & A_{PS}(\theta,\varphi) \\ A_{SP}(\theta,\varphi) & A_{PP}(\theta,\varphi) \end{bmatrix} \cdot \begin{bmatrix} I_{xs}(\theta,\varphi) & I_{ys}(\theta,\varphi) \\ I_{xp}(\theta,\varphi) & I_{yp}(\theta,\varphi) \end{bmatrix} \cdot \begin{bmatrix} Ex \\ Ey \end{bmatrix}. \quad (1)$$

The analyzer matrix $\begin{bmatrix} A_{SS}(\theta,\varphi) & A_{PS}(\theta,\varphi) \\ A_{SP}(\theta,\varphi) & A_{PP}(\theta,\varphi) \end{bmatrix}$ is characterized on the bench top as a function of zenith angle θ and azimuth angle φ. Its four components correspond to the *ss*, *sp*, *ps*, and *pp* polarizer-analyzer combinations. The photodiode is also characterized on the bench as a function of angle in order to get the PD matrix $\begin{bmatrix} PD_{SS}(\theta,\varphi) & 0 \\ 0 & PD_{PP}(\theta,\varphi) \end{bmatrix}$. Then, a mirror or silicon surface is placed at the sample plane and the intensity from these same four polarization states are acquired at the CCD image detector through the complete path, $I_{CCD-xx}(\theta,\varphi)$, $I_{CCD-xy}(\theta,\varphi)$, $I_{CCD-yx}(\theta,\varphi)$, and $I_{CCD-yy}(\theta,\varphi)$, where

Downloaded From: http://proceedings.spiedigitallibrary.org/ on 10/15/2012 Terms of Use: http://spiedl.org/terms

$$\begin{bmatrix} \sqrt{I_{CCD-xx}(\theta,\varphi)} & \sqrt{I_{CCD-yx}(\theta,\varphi)} \\ \sqrt{I_{CCD-xy}(\theta,\varphi)} & \sqrt{I_{CCD-yy}(\theta,\varphi)} \end{bmatrix} =$$

$$\begin{bmatrix} A_{xx} & A_{yx} \\ A_{xy} & A_{yy} \end{bmatrix} \cdot \begin{bmatrix} C_{sx}(\theta,\varphi) & C_{px}(\theta,\varphi) \\ C_{sy}(\theta,\varphi) & C_{py}(\theta,\varphi) \end{bmatrix} \cdot \begin{bmatrix} R_{ref-ss}(\theta,\varphi) & R_{ref-ps}(\theta,\varphi) \\ R_{ref-sp}(\theta,\varphi) & R_{ref-pp}(\theta,\varphi) \end{bmatrix} \cdot \begin{bmatrix} I_{xs}(\theta,\varphi) & I_{ys}(\theta,\varphi) \\ I_{xp}(\theta,\varphi) & I_{yp}(\theta,\varphi) \end{bmatrix} \cdot \begin{bmatrix} Ex \\ Ey \end{bmatrix}. \quad (2)$$

Here, $\begin{bmatrix} Ex \\ Ey \end{bmatrix}$ is either $\begin{bmatrix} 1 \\ 0 \end{bmatrix}$ or $\begin{bmatrix} 0 \\ 1 \end{bmatrix}$, and $\begin{bmatrix} A_{xx} & A_{yx} \\ A_{xy} & A_{yy} \end{bmatrix}$ is either $\begin{bmatrix} 1 & 0 \\ 0 & 0 \end{bmatrix}$, $\begin{bmatrix} 0 & 0 \\ 0 & 1 \end{bmatrix}$. Through matrix calculation, we can determine the illumination path tool function $\begin{bmatrix} I_{xs}(\theta,\varphi) & I_{ys}(\theta,\varphi) \\ I_{xp}(\theta,\varphi) & I_{yp}(\theta,\varphi) \end{bmatrix}$. The collection path tool function, $\begin{bmatrix} C_{sx}(\theta,\varphi) & C_{px}(\theta,\varphi) \\ C_{sy}(\theta,\varphi) & C_{py}(\theta,\varphi) \end{bmatrix}$, is not measured directly but is obtained by dividing and the complete pass tool function by the illumination path tool function as shown in Fig. 3.

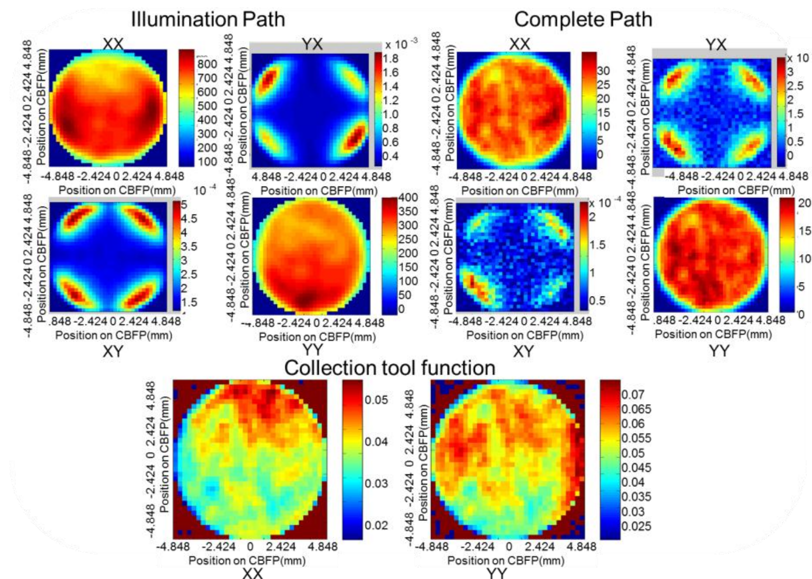

Figure 3. Maps for the four polarizer-analyzer combinations for each point in the conjugate back focal plane for the illumination path tool function and complete path function matrices. The color bars for the illumination and complete path are intensities with CCD units, and the color scales on the cross terms (XY and YX) are not the same as for the other plots. The color bars for collection tool function show the transmissivity of the collection path.

As the cross-polarization terms in the illumination and complete tool functions are 10^{-3} times smaller than the other two terms, they were not used in determining the collection tool function.

Once the illumination and collection functions have been acquired for the entire range of angles and polarization states, a new approach must be taken to normalize the scattered field in the frequency domain. The incident illumination is first independently normalized by the illumination path tool function. The collection path normalization is accomplished by applying the collection path tool function to the simulated scattered frequency components before the simulation image is constructed at the image plane, shown schematically on the left in Fig. 4. After the image is reconstructed, parametric fitting is carried out.

Downloaded From: http://proceedings.spiedigitallibrary.org/ on 10/15/2012 Terms of Use: http://spiedl.org/terms

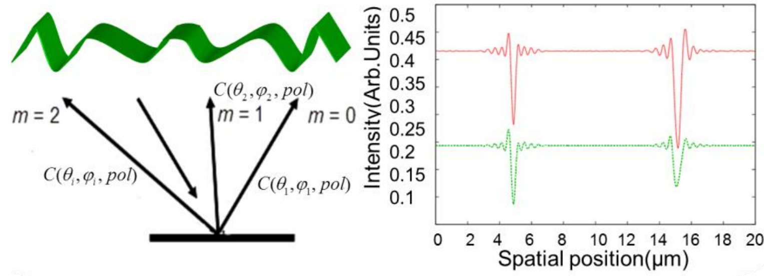

Figure 4. Method for tool normalization when high order scattered light is present. Both scattered light angles and polarization states need to be correctly normalized. The red curve shows uncorrected simulation data and the green shows the reconstructed image after Fourier normalization.

Great care needs to be taken to quantify and account for the off-axis behavior of the system, and this is particularly challenging as the detectors and polarizers have non-optimum behavior at oblique, off-axis angles of incidence.

3. REGRESSION ANALYSIS AND SIMULATION STUDIES

We now develop a nonlinear regression model applicable to a set of images. Although the model can be expanded using a Bayesian approach to include *a priori* information for hybrid metrology, we only employ a single measurement tool in this paper. Only an overview to the initial derivation is given here, see Refs. 4, 8, and 9 for a more detailed formalism.

In general a complete set of measurements consists of N data points acquired under a varying set of conditions for both simulations and experimental measurements. The K model parameters are expressed as a vector $\mathbf{a} = \{a_1, ..., a_K\}$, and represent the model input parameters, for example, CD, sidewall, height. We have N measured values of Y denoted as $\{y_1, ..., y_N\}$ and N simulated values $y(x_i;\mathbf{a})$ corresponding to the ith data point x_i. We want to compare the measured $\{y_1, ..., y_N\}$ with simulated $\{y(x_i;\mathbf{a})\}, i = 1, ..., N\}$ and find an optimal estimator of the parameter vector $\mathbf{a} = \{a_1, ..., a_K\}$. In general, $y(x_i;\mathbf{a})$ is a nonlinear function of $\mathbf{a}$. Treating $y(x_i;\mathbf{a})$ as a mean response of y_i, and by using a first-order Taylor expansion, a linear approximation of the nonlinear regression for y_i is given by

$$y_i = y(x_i;\mathbf{a}(0)) + \sum_{k=1}^{K} \left[\frac{\partial y(x_i;\mathbf{a})}{\partial a_k} \right]_{\mathbf{a}=\mathbf{a}(0)} (a_k - a_k(0)) + \varepsilon_i , \quad (3)$$

where $\mathbf{a}(0) = \{a_1(0), ..., a_K(0)\}$) is an initial value or an optimal value of $\mathbf{a}$ and ε_i is the corresponding random error with zero mean [10]. By re-parameterization, the model can be expressed as

$$y_i(0) = \sum_{k=1}^{K} D_{ik}(0)\beta_k(0) + \varepsilon_i , \quad (4)$$

with $\beta_k(0) = a_k - a_k(0)$ and $y_i(0) = y_i - y(x_i;\mathbf{a}(0))$. The covariance matrix of the experimental values $\{y_1, ..., y_N\}$ is denoted by $\mathbf{V} = diag[\sigma_1^2, ..., \sigma_N^2]$. We can now write the re-parameterized model from Eqn. 4 in a matrix form,

$$\mathbf{Y}(0) = \mathbf{D(0)}\boldsymbol{\beta}(0) + \boldsymbol{\varepsilon} \quad . \quad (5)$$

Downloaded From: http://proceedings.spiedigitallibrary.org/ on 10/15/2012 Terms of Use: http://spiedl.org/terms

It can be shown [9,11] that the generalized least squares estimator of $\boldsymbol{\beta}(0)$ is now given by

$$\hat{\boldsymbol{\beta}}(0) = \left(\mathbf{D(0)}^{\mathbf{T}}\mathbf{V}^{\mathbf{-1}}\mathbf{D(0)}\right)^{\mathbf{-1}}\mathbf{D(0)}^{\mathbf{T}}\mathbf{V}^{\mathbf{-1}}\mathbf{Y(0)}\,, \tag{6}$$

where $\hat{\boldsymbol{\beta}}(0) = (\hat{\beta}_1(0),\ldots,\hat{\beta}_K(0))$ are the best linear unbiased estimators of $\boldsymbol{\beta}(0)$, from which we can get the best estimators of parameter $\mathbf{a}$. In the regression approach outlined above, we concatenate the data from each experimental profile into one data string and solve for the best parameter fit and parametric uncertainties as we have previously outlined.

Before applying this approach to experimental data sets, a simulation based study was carried out to evaluate this technique for CD metrology for isolated dense array targets with decreased uncertainty. We added a noise profile that contains both realistic systematic errors and random noise, shown in Fig. 5, to a simulated image that was chosen from a central location in the simulation library space. This noise-laden simulation set is then treated as the "experimental" data set to be fit. Then we concatenated all data sets from different focus positions or from different incident angles as one data string, on which a standard regression analysis is done and uncertainty is calculated. This is done to enable modeling comparisons of the edges of a finite scatterometry target, as well as a baseline calibration for both the nearby substrate and the dense specular or high-order optical response from the linearly arrayed region.

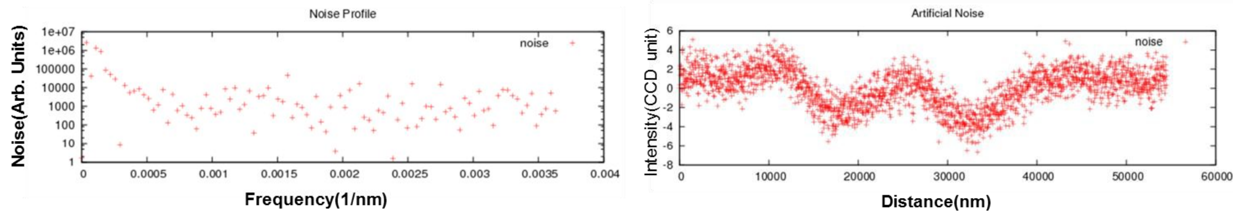

Figure 5. (a) Realistic noise spectrum based on experimental data. (b) One example of a noise profile based on the noise spectrum from (a). This noise is added to a simulation to emulate an "experimental" curve.

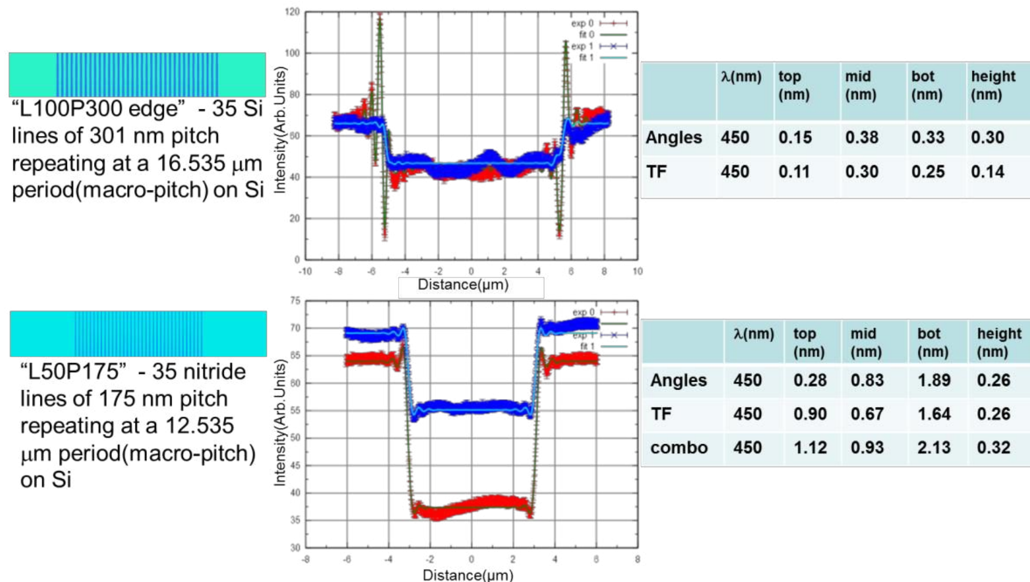

	λ(nm)	top (nm)	mid (nm)	bot (nm)	height (nm)
Angles	450	0.15	0.38	0.33	0.30
TF	450	0.11	0.30	0.25	0.14

	λ(nm)	top (nm)	mid (nm)	bot (nm)	height (nm)
Angles	450	0.28	0.83	1.89	0.26
TF	450	0.90	0.67	1.64	0.26
combo	450	1.12	0.93	2.13	0.32

Figure 6. Two simulation studies for finite gratings simulated using RCWA. Each angle scan or through-focus scan consists of 84 concatenated profiles. The center graphics each show the best fit simulation curves for given "experimental" (noise-added simulation) curves for two polarizations at a selected focus or angle position. Concatenating selected angle scans and through focus (TF) scans (78 profiles), shown as "combo" in the table, does not reduce the parametric uncertainties comparing to angle-only and TF-only technique.

Downloaded From: http://proceedings.spiedigitallibrary.org/ on 10/15/2012 Terms of Use: http://spiedl.org/terms

Our scattering simulation methods include a finite difference time domain (FDTD) approach and a rigorous coupled waveguide analysis model (RCWA) [12], both of which were developed in house. In-house model development is critically important as significant modification of the Fourier optical simulation components were required. In Fig. 6, on the left, is shown the nominal target geometry including the CD, number of lines, and the pitch as well as the macro-pitch. The macro-pitch is the period over which the finite grating is repeated in the numerical simulations while the lines are infinite in length for these simulations. In the center part of the figure, examples of the simulated “experimental” curves are overlaid with the best fit curves from the simulation library. On the right, the standard 1σ parametric fitting uncertainties are shown for the four floated parameters for both through-focus and angle-resolved analysis.

These data are for the “L100P300” finite arrays in the upper portion and “L50P175” in the lower part of the figure, denoting 100 nm and 50 nm linewidths and 300 nm and 175 nm pitches, respectively. The macro-pitch for the simulation of these particular targets are chosen to be large enough that the array edges are “isolated” from interacting optically with periodic copies of the array, and we chose 35 lines in the array so that the central region reaches its nominal steady state optical response for an infinite array. Phase interactions among lines near the array edge contribute to the scattered field of the edge, so that the transition between the “infinite” grating and the edge contains significant measurable information.

The uncertainties are again based on the noise profiles shown in Fig. 5 and are realistic if not overly conservative. One concern when measuring finite arrays as measured above is that the outermost edge may have an inordinately large effect on the scattered profile and potentially dominate the signal. We have investigated this possibility in simulation and the conclusion is that the outer most edge has an effect approximately inversely proportional to the number of lines that scatter high order light [5]. On further investigation, the data show that in the middle of a sufficiently large array, a steady state scattered signal is achieved mid array, however, as one approaches the edge, the scattered light transitions from diffraction grating behavior to isolated feature behavior with a continuum of spatial frequency information. The image content and frequency information is not dominated by the outer most features. There is a transition from an array optical response to more of an isolated feature behavior with broad optical content. These simulation results will be published in the future.

4. EXPERIMENTAL SENSITIVITIES

An experimental sensitivity analysis was carried out to validate and quantify the observed sensitivity as well as for subsequent theory-to-experiment comparisons. Accurate comparisons with minimal residuals are essential to develop quantitative modeling and an independent measurement capability. Two types of targets were measured, We use a array of lines with 100 nm CD and 600 nm pitch which is referred to as the “L100P600” target. We also used an array of lines with 100 nm CD and 300 nm pitch. With λ=450 nm, the L100P600 target exhibits multiple scattering orders while the L100P300 gives only 0th-order scattering. Measurements of the L100600 were conducted near the middle of the array, filling the FOV. The L100P300 was measured along one edge of the array, to test sensitivity at the edge of a finite array. Each type of target is printed using a focus exposure matrix (FEM) providing a series of die with linewidth and sidewall profiles that vary on the nanometer scale.

The L100P600 targets are of particular interest as they contain only *m =-1, 0* and *+1* orders at normal incidence although the 2_{nd} order can be rocked in at high angles. Figure 7 shows x and y polarization with several panels at varying focus slices. Each panel at a given focus position shows eight profiles plotted together that correspond to eight different CD values each acquired at a different die. For each polarization the figure shows ten sets of plots with each set of profiles acquired at focus positions from 400 nm above the substrate to 500 nm below substrate in 100 nm increments.

Enlargements of the best focus panels from Fig. 7 are shown in Fig. 8, where the profiles from the eight die that were plotted together can be seen clearly. The σ_{repeat} values in the figure are the range of repeatabilities for each data point scaled to the figures as labeled. The FEM resulted in the eight die having a nominal variation in middle linewidth of 10 nm ranging from 115 nm to 125 nm and sidewall variations of ranging from 5° to 8°, which result in curve differences on the 10^{-2} scale with each curve having a σ_{repeat} on the 10^{-3} scale, as shown in Fig. 8, thus demonstrating good sensitivity to the nanometer scale changes in linewidth for the focus-resolved experiments.

Downloaded From: http://proceedings.spiedigitallibrary.org/ on 10/15/2012 Terms of Use: http://spiedl.org/terms

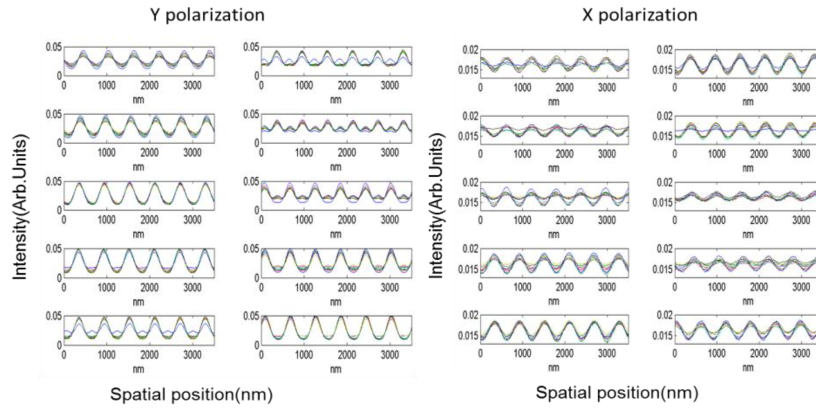

Figure 7. Experimental focus-resolved L100P600 lines. The left side and right side data sets show profiles acquired from 400 nm above the substrate to 500 nm below in 100 nm increments.

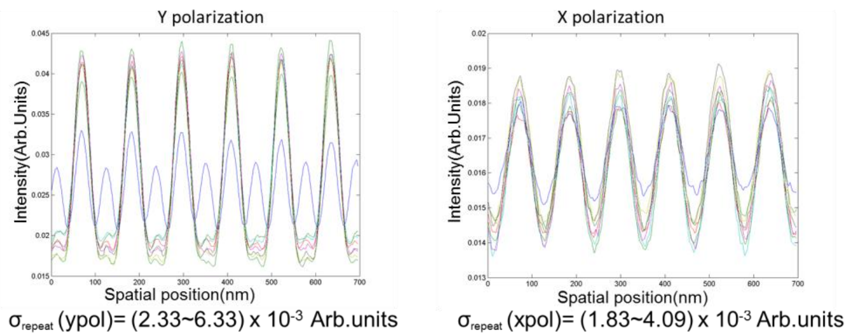

Figure 8. Enlargement of the best focus panel in Fig. 7.

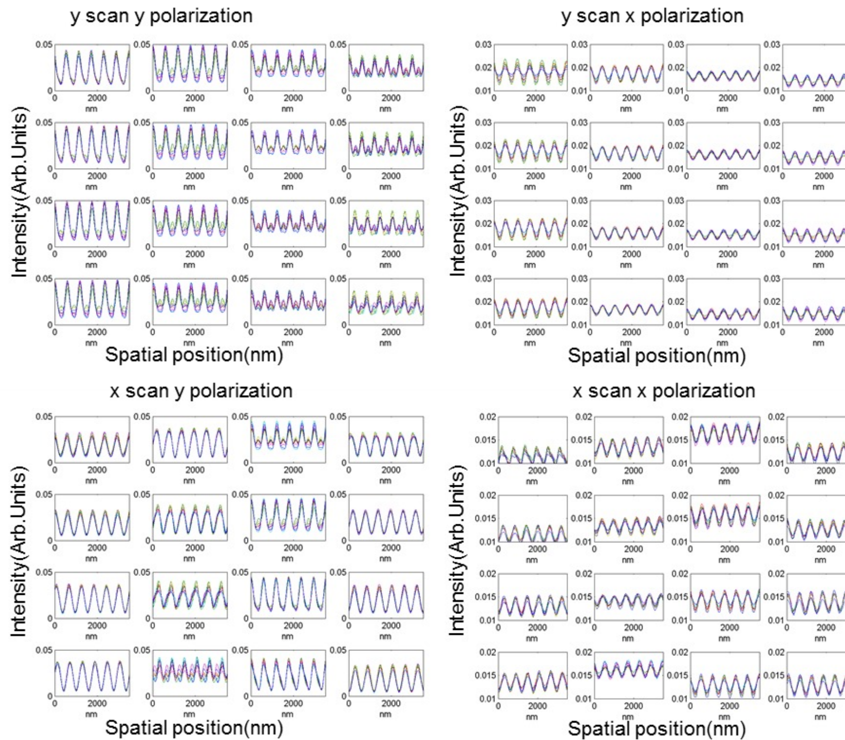

Figure 9. Experimental angle-resolved L100P600 lines. From left side to right side data sets show profiles acquired at y_{scan},y_{pol}; y_{scan},x_{pol}; x_{scan},y_{pol}; and x_{scan},x_{pol}.

Downloaded From: http://proceedings.spiedigitallibrary.org/ on 10/15/2012 Terms of Use: http://spiedl.org/terms

Angle-resolved experiments for L100P600 show similar sensitivity. Fig. 9 shows four groups of results with y_{scan},y_{pol}; y_{scan},x_{pol}; x_{scan},y_{pol}; and x_{scan},x_{pol}, with several panels showing profiles measured at various incident angles at the best focus position. Each panel at a given incident angle shows eight profiles plotted together that correspond to eight different CD values each acquired at a different die.

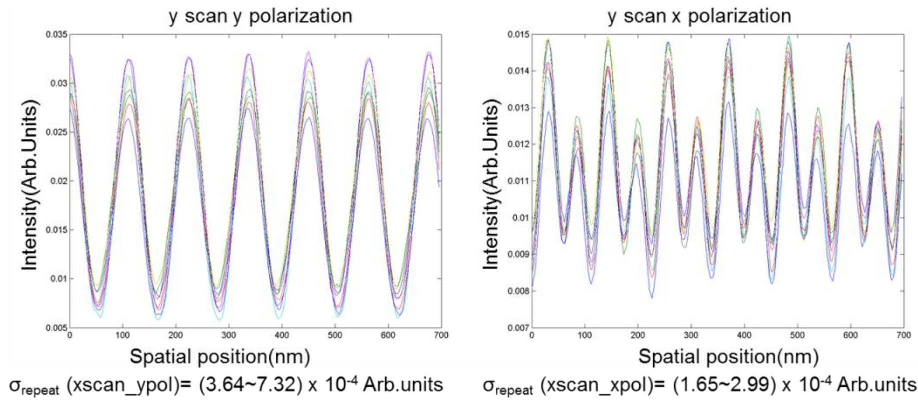

Figure 10. Enlargement of angle-resolved experimental data for L100P600 lines from Fig. 9.

In Fig. 10, the two graphs show sets of image profiles acquired at a given angle and at best focus, each showing eight profiles for the eight die. The σ_{repeat} values are again the range of repeatabilities for each data point scaled to the figures as labeled and the eight die are the same as used for the L100P600 data above. Again, with curve differences on the 10^{-2} scale and each curve having a σ_{repeat} on the 10^{-3} scale, very good sensitivity to the linewidth variations are observed as a function of angle.

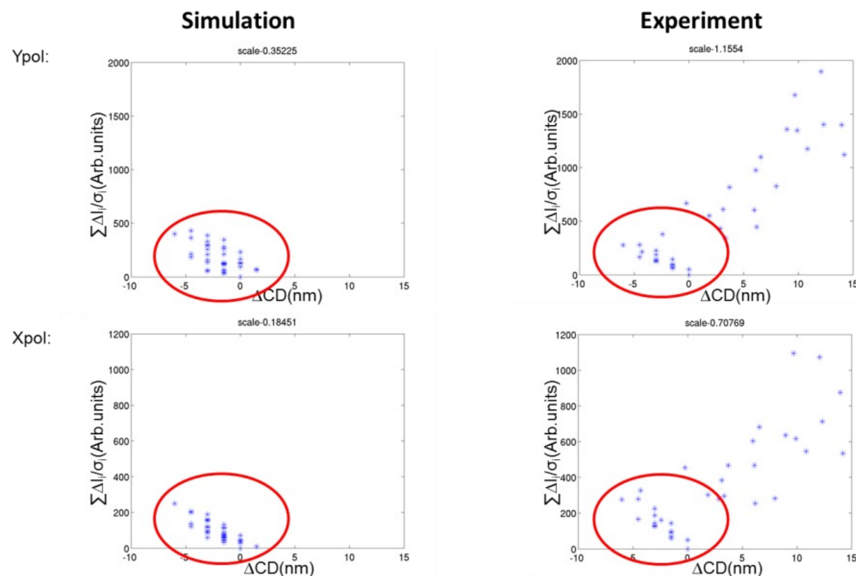

Figure 11. Sensitivity matrix plots for L100P300 target for both simulation data and experimental data.

We also did a separate sensitivity test, measuring the edge of the L100P300 dense line array target. Angle-resolved sensitivities are shown in Fig. 11. Sensitivity for multiple incident angles is plotted as a function of change in line width for both simulation and experiments. The scattered pattern in the vertical direction corresponds to various incident angles. Comparison of sensitivities show qualitative agreement between experiments and simulation in the regions marked with red circles.

Downloaded From: http://proceedings.spiedigitallibrary.org/ on 10/15/2012 Terms of Use: http://spiedl.org/terms

5. PARAMETRIC FITTING RESULTS WITH UNCERTAINTY ANALYSIS

In this section we show a comparison of experimental data with theoretical simulations for two targets. For the L100P600 target, we define the model with four parameters: top width, middle width, bottom width, and height. This is not an isolated target as it fills the FOV, however it provides an important test of the modeling and normalization method as it scatters well-defined scattering orders and there is substantial through-focus phase contrast and intensity variation. In Fig. 12 two polarizations are shown at normal incidence for four different focus positions with 100 nm increments. This uses the full Fourier normalization approach for the illumination path tool function and the collection path tool function applied to the scattered orders, as described in Section 2.

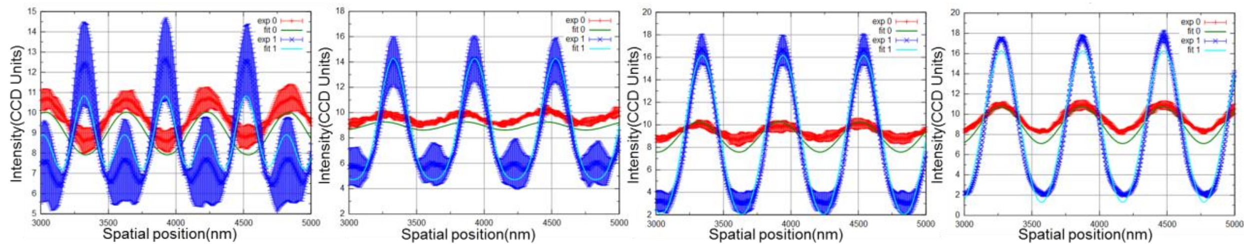

Figure 12. Focus-resolved theory to experiment comparisons of the L100P600 target. The focus was varied in 100 nm increments between panels. Two different polarizations are shown in each graph.

Another important and challenging test for this methodology is the measurement of a single Si edge since an edge scatters a continuum of spatial frequencies. The simulations are performed with a model that is described by two parameters: height and sidewall angle. We fit experimental data to normalized simulation data throughout the entire library, obtaining a best fit with a height of 228 nm and a sidewall angle of 2°. Figure 13 shows the entire fitting results through a 4 μm focus range, from 2 μm below the best focus to 2 μm above the best focus in 200 nm increments. Best focus is defined here using a Focus Matrix (FM) algorithm separately for each polarization, which is the integration of the gradient along the bottom peak of these profiles. The FM curves show a more than 1 μm difference on best focus position between the x and y polarizations, as shown in Fig. 14. This shift is most likely the result of the microscope beam splitter, which is made of a material with inhomogeneous retardance. This will be characterized in detail in future work, and treated as a systematic error.

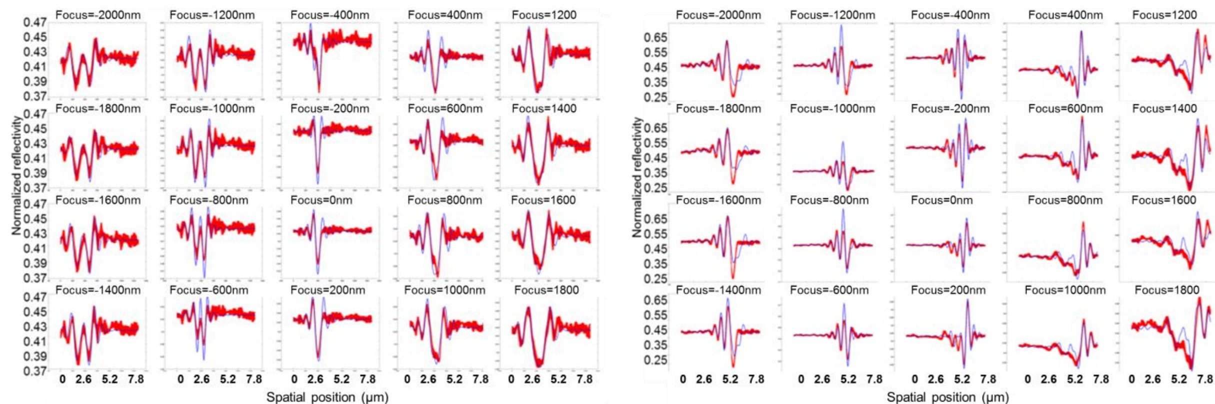

Figure 13. Focus-resolved theory-to-experiment comparisons of the Si single edge target. The focus was varied in 200 nm increments between panels, and 20 panels in total shows focus positions vary from 2 μm below best focus to 2 μm above best focus. Left is for x polarization, and right is for y polarization.

The error bars shown in Fig. 13 only account for type A repeatability errors. Type B errors, such as systematic hardware errors, tool function error, and the phase error that can vary between different spatial frequencies, have not been fully considered in this example. Even so, we can still see a consistent theory-to-experiment agreement here throughout the entire 4 μm range. The fitting results for x polarization are shown in the left group of figures and y polarization are shown in the right group of figures. They are plotted on different scales, as x polarization profiles vary over a smaller

Downloaded From: http://proceedings.spiedigitallibrary.org/ on 10/15/2012 Terms of Use: http://spiedl.org/terms

normalized reflectivity range than those for the y polarization. Though it changes over a smaller range, the x polarization shows more sensitivity to the changes of CD, based on shape changes in this example, than those for y polarization.

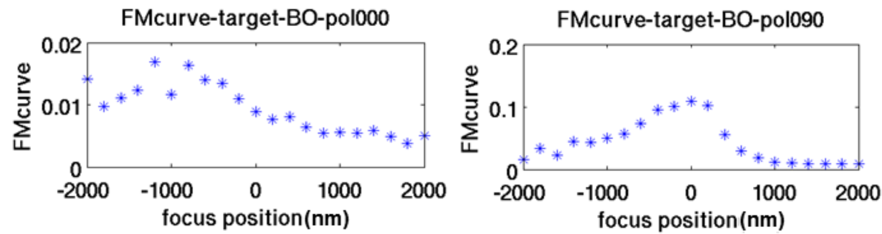

Figure 14. FM curves for both x polarization (left) and y polarization (right).

In Fig. 15, we selected eight images at different focus positions from Fig. 13 with increased error bars that are estimates to cover type B errors as well as errors that might be caused by phase errors which have not yet been fully characterized. After the regression analysis, we calculate that the parametric uncertainty for height and side wall angle are 0.08 nm and 0.03°, which is quite small, the direct result of virtually no correlation between these two parameters and that the experimental data show great sensitivity through the range of focus. The experimental data and the simulation studies show that the fundamental basis for decreased uncertainties using these techniques is valid.

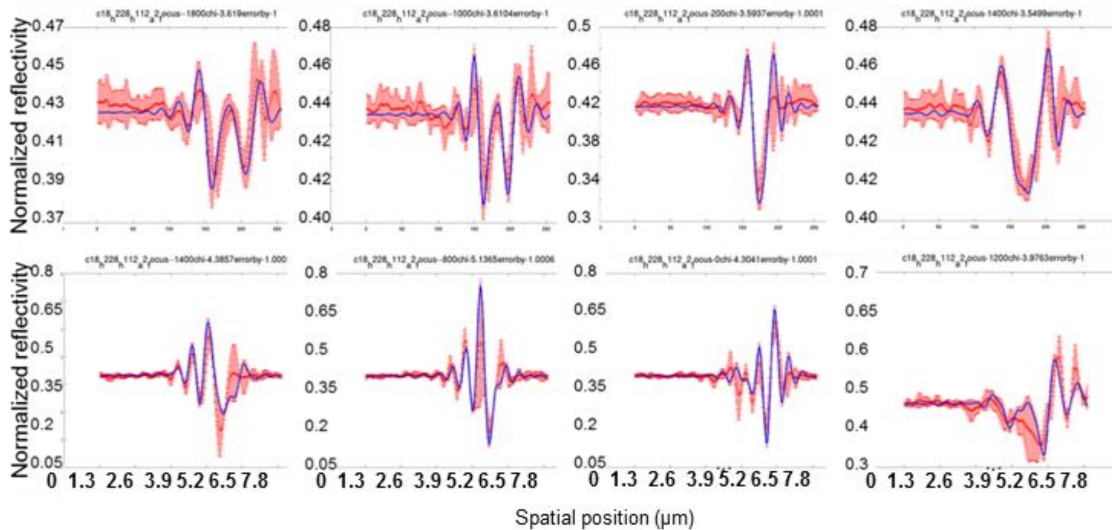

Figure 15. Example focus-resolved theory-to-experiment fitting results of the Si single edge target, with increased error bars.

6. CONCLUSION

Using accurate optical tool characterization and frequency domain normalization, a path to quantitative modeling was demonstrated for targets with a scattered electromagnetic field containing multiple spatial frequencies. Both the modeling and experimental data demonstrate that nanometer-scale measurements can be achieved using angle-resolved or focus-resolved scatterfield microscopy. Sensitivity was demonstrated in measurements of the edge of a dense line array as well as isolated targets with higher order diffracted light. A sophisticated approach must be applied in the Fourier domain that corrects optical path errors in both the illumination and collection path throughout the angular spectrum as a function of polarization. With this approach, both the L100P600 and single Si edge targets show consistent theory-to-experiment fitting results throughout a wide focal range. By concatenating image-based profiles from several focus heights into a single data string and performing a rigorous regression analysis against a library of physics-based simulations, we can potentially decrease parametric uncertainty to the sub-nanometer scale. Analyzing Type A and estimating Type B uncertainty components, sub-nanometer parametric uncertainties were obtained. These

Downloaded From: http://proceedings.spiedigitallibrary.org/ on 10/15/2012 Terms of Use: http://spiedl.org/terms

results suggest a potential new basis for the quantitative measurement of targets having finite, sub-FOV overall dimensions. While single targets were measured in this paper, this methodology is extensible to parallel measurements of multiple targets, potentially enabling in-chip applications for both CD and overlay metrology.

ACKNOWLEDGEMENTS

The authors would like to thank SEMATECH for wafer fabrication and measurement support. The authors wish to thank Thomas Germer for providing a 2-D RCWA code and are indebted to Nien-Fan Zhang for research in developing the regression analysis and Bayesian statistical methods.

REFERENCES

[1] Silver. R. M., Barnes, B., Attota, R., Jun, J., Stocker, M., Marx, E., and Patrick, H., "Scatterfield Microscopy to Extend the Limits of Image-based Optical Metrology," Applied Optics, 46, 20, pp. 4248-4257 (2007).
[2] Patrick, H., Attota, R., Barnes, B., Germer, T., Dixson, R.G., Stocker, M., Silver, R. M. and Bishop, M., "Optical Critical Dimension Measurement of Silicon Grating Targets using Back Focal Plane Scatterfield Microscopy," J Micor/Nanolith., MEMS and MOEMS 7(1), 0137011, (2007).
[3] Barnes, B. M., Howard, L.P., Jun J., Lipscomb, P. and Silver, R.M., "Zero-order imaging of device-sized overlay targets using scatterfield microscopy," Proc. SPIE 6518, 65180F (2007).
[4] Silver, R. M., Zhang, N. F., Barnes, B., Zhou, H., Heckert, A., Dixson, R., Germer, T. and Bunday, B., "Improving optical measurement accuracy using multi-technique nested uncertainties," Proc. SPIE 7272, 727202 (2009).
[5] Silver, R. M., Qin, J., Barnes, B. M., Zhou, H., Dixson, R. and Goasmat, F., "Phase sensitive parametric optical metrology: exploring the limits of three-dimensional optical metrology," Proc. SPIE 8324, 83240N (2012).
[6] Sohn, Y. J., Barnes, B. M., Howard, L., Silver, R. M., Attota, R. and Stocker, M.T., "Koehler illumination in high-resolution optical metrology," Proc. SPIE. 6152, 61523S (2006)
[7] Barnes, B.M., Attota, R., Quintanilha, R., Sohn, Y. J. and Silver, R.M, "Characterizing a scatterfield optical platform for semiconductor metrology," Meas. Sci. Technol. 22, 024003 (2012).
[8] Silver, R. M., Zhang, N. F., Barnes, B., Zhou, H., Qin, J. and Dixson, R., "Nested Uncertainties to Improve Measurement Accuracy," Proc. SPIE 7971, 797116 (2011).
[9] Zhang, N. F., Silver, R. M., Zhou, H. and Barnes, B. M., "Improving optical measurement uncertainty with combined multitool metrology using a Bayesian approach," Appl. Opt. 51, 6196-6206 (2012).
[10] Neter, J., Wasserman, W. and Kutner, M., [Applied Linear Regression Models,] Richard D. Irwin, Inc, Homewood, Illinois, (1983).
[11] Rao, C. R. and Toutenburg, H., [Linear Models: Least squares and Alternatives,] Springer, (1995).
[12] Moharam, M. G., Pommet, D. A., Grann, E. B. and Gaylord, T. K., "Stable implementation of the rigorous coupled wave analysis for surface-relief gratings: enhanced transmittance matrix approach," J. Opt. Soc. Am. A 12, 1077-1086 (1995).

Downloaded From: http://proceedings.spiedigitallibrary.org/ on 10/15/2012 Terms of Use: http://spiedl.org/terms